Accepted JGR Space Physics, 16 April 2020 https://doi.org/10.1029/2019JA027442

Influence of He^{++} and shock geometry on interplanetary shocks in the solar wind: 2D Hybrid simulations

L. Preisser,[1] X. Blanco-Cano,[1] D. Trotta,[2] D. Burgess,[2] and P. Kajdič [1]

[1] Instituto de Geofísica, Universidad Nacional Autónoma de México, Circuito de la investigación Científica s/n, Ciudad Universitaria, Delegación Coyoacán, C.P. 04510, Mexico City, Mexico
[2] School of Physics and Astronomy, Queen Mary University of London, London E1 4NS, UK

Key Points:

- He++ content modifies the shock profile, temperature anisotropy and distribution functions in the upstream and downstream regions.
- θ_{Bn} and He++ content affects the efficiency with which particles escape to the upstream region.
- Increase in magnetic fluctuations and He++ content modify regions with higher temperature anisotropy downstream of quasi-perpendicular shocks.

Corresponding author: L. Preisser, preisser@igeofisica.unam.mx

Abstract

After protons, alpha particles (He^{++}) are the most important ion species in the solar wind, constituting typically about 5% of the total ion number density. Due to their different charge-to-mass ratio protons and He^{++} particles are accelerated differently when they cross the electrostatic potential in a collisionless shock. This behavior can produce changes in the velocity distribution function (VDF) for both species generating anisotropy in the temperature which is considered to be the energy source for various phenomena such as ion cyclotron and mirror mode waves. How these changes in temperature anisotropy and shock structure depend on the percentage of He^{++} particles and the geometry of the shock is not completely understood. In this paper we have performed various 2D local hybrid simulations (particle ions, massless fluid electrons) with similar characteristics (e.g., Mach number) to interplanetary shocks for both quasi-parallel and quasi-perpendicular geometries self-consistently including different percentages of He^{++} particles. We have found changes in the shock transition behavior as well as in the temperature anisotropy as functions of both the shock geometry and He^{++} particle abundance: The change of the initial θ_{Bn} leads to variations of the efficiency with which particles can escape to the upstream region facilitating or not the formation of compressive structures in the magnetic field that will produce increments in perpendicular temperature. The regions where both temperature anisotropy and compressive fluctuations appear tend to be more extended and reach higher values as the He^{++} content in the simulations increases.

1 Introduction

Collisionless shocks are a phenomenon of crucial importance in heliospheric/space plasma physics and astrophysics. Along with solar flares they are the main particle accelerators near the Sun and in the interplanetary (IP) medium. The energy dissipation produced by collisionless shocks is a complex consequence of the interaction between particles and the electric and magnetic fields at the shock interface together with wave-particle interactions in the wave field driven by instabilities at the shock and in the upstream and downstream regions. In addition, due to the lack of collisions, a small fraction of particles can be reflected towards the upstream side of the shocks, reaching high energies [*Gosling & Thomsen*, 1985; *Gosling et al.*, 1989; *Burgess & Scholer*, 2015].

Depending on the shock normal angle θ_{Bn}, defined as the angle between the upstream magnetic field and the shock normal direction, collisionless shocks can be divided in two types: quasi-parallel ($\theta_{Bn} < 45°$) and quasi-perpendicular ($\theta_{Bn} > 45°$). Ion acceleration at the shock can be caused by different processes: shock drift acceleration [*Burgess*, 1987a] is usually considered to be the main mechanism operating in quasi-perpendicular shocks, while diffusive shock acceleration [*Blanford & Ostriker*, 1978] works more efficiently in quasi-parallel shocks [see *Burgess & Scholer*, 2015, for a detailed description].

In quasi-parallel shocks, the reflected ions can escape back to the upstream side along the magnetic field lines where their interaction with the solar wind (SW) particles can lead to excitation of upstream waves including ultra-low-frequency (ULF) waves which can evolve into shocklets, and other large-amplitude magnetic structures [*Russell & Hoppe*, 1983; *Blanco-Cano et al.*, 2016; *Wilson, L. B. III*, 2016]. Consequently, the region upstream of a quasi-parallel shock is intimately linked to the generation of high-energy upstream ions, and is in particular related to the extraction of thermal particles from the upstream side of the shock into the population of energetic ions [*Scholer & Burgess*, 1992; *Burgess et al.*, 2005; *Su et al.*, 2012a,b; *Sundberg et al.*, 2016].

In quasi-perpendicular shocks, the specularly reflected ions gyrate in the upstream magnetic field generating a foot region, penetrating the shock potential back to the downstream side with high tangential velocities, producing an anisotropic distribution with the perpendicular temperature larger than the parallel one near the shock front. Linear theory and simulations have shown that such an anisotropic distribution can be unstable to ion cyclotron and mirror mode waves [*Gary*, 1993; *Lembège & Savoini*, 1992; *Hada et al.*, 2003; *Yang et al.*, 2009, 2012]. These waves have been observed in the Earth's magnetosheath behind the quasi-perpendicular bow shock [*Anderson & Fuselier*, 1993], downstream of shocks associated to stream interaction regions (SIRs) [*Blanco-Cano* *et al.*, 2016] and also in complex events formed by two or more large-scale solar wind structures which interact in the interplanetary space [*Enriquez-Rivera et al.*, 2010, 2013; *Siu-Tapia et al.*, 2015].

In the solar wind, the shock interface conditions are basically determined by the dynamics of protons, which are the most abundant ion species. However, there are also various kinds of minor ions. Among these, He^{++} is the most important ion species and although it constitutes typically only about 4-5% of the total ion number density [*Neugebauer & Snyder*, 1966; *Ipavich et al.*, 1984; *Wurz*, 2005], its contribution to the upstream mass density and dynamical pressure can be as large as 20%. Therefore, He^{++} effects in shock dynamics should not be ignored as has been pointed previously [*Geiss et al.*, 1970; *Kasper et al.*, 2007; *Gedalin*, 2017].

One of the most interesting features that hybrid simulations of quasi-parallel shocks have revealed is a cyclic behavior [*Burgess*, 1989a] in their structure above an Alfvénic Mach number of $M_A = V_u/V_A \sim 2$: upstream waves are convected towards the shock, being compressed as they approach producing a gradual shock profile. These arriving waves steepen up at the upstream edge which becomes the newly reformed shock [*Burgess*, 1989a; *Scholer & Terasawa*, 1990; *Hao et al.*, 2016]. In 1D simulations of quasi-parallel shocks with $\theta_{Bn} \gtrsim 20°$ the low frequency upstream waves evolve to large amplitude pulsations very close to the shock to later interact with the shock, producing an associated increased density of diffuse and/or nearly specularly reflected ions. At 1 AU the observations of interplanetary shocks show different micro-structure even for similar θ_{Bn} values [*Blanco-Cano et al.*, 2016; *Kajdič et al.*, 2012]. This can be attributed to time evolution of the shock front and/or local geometry irregularities, which have been reported and studied at different spatial scales via multispacecraft analysis and hybrid simulations [*Aguilar-Rodriguez et al.*, 2011; *Kajdič et al.*, 2019].

In the past, quasi-parallel hybrid simulations with He^{++}as second heavy ion species have been performed [*Trattner & Scholer*, 1991, 1994], showing that solar wind alpha particles penetrate the shock ramp rather unaffected and gyrate in the downstream magnetic field. In the case of low (~ 0.1) upstream β (ratio of thermal to magnetic pressures) this gyration is in general well behind the shock ramp, and no diffuse alpha particles are generated. However, occasionally the whole distribution is able to gyrate back to the shock ramp and gets accelerated into the upstream region by the electric field in the shock ramp. This leads to the formation of localized backstreaming He^{++} clouds which are the source of diffuse alpha particles. At higher Mach number ($M_A \sim 9$), the gyroradii increase which makes it easier for the beam-like alpha particles behind the shock to reach the shock ramp for a second time. This causes a strong increase of the number of backstreaming alpha particles. *Trattner & Scholer* (1993) performed 1D hybrid simulations with different alpha particles to proton ratio. Assuming an upstream alpha particle-to-proton temperature ratio (T_α/T_p) of 4, the downstream temperature ratio of alpha particles to protons was enhanced ($\sim$ 5-7). In a recent work [*Caprioli et al.*, 2017] has studied the thermalization, injection, and acceleration of ions with different mass/charge ratios (A/Z) in non-relativistic collisionless shocks via hybrid simulations finding that in general, ions thermalize to a post-shock temperature proportional to A. When diffusive shock acceleration was efficient, the ions develop a non-thermal tail whose extent scales with Z, so that incompletely-ionized heavy ions are preferentially accelerated.

Various works concerning quasi-perpendicular shock hybrid simulations including He^{++} ions [*McKean et al.*, 1995a, 1996] have been carried out in order to study the wave evolution in the downstream region for low and high Mach number (M_A) shocks. These works show how the proton cyclotron and mirror mode waves can be excited near the shock front to be convected further downstream. The energy of the proton cyclotron waves driven by the proton temperature anisotropy $T_\perp/T_\parallel > 1$ [e.g., *Gary et al.*, 1996] can be absorbed by the He^{++} particles leading to thermalized He^{++} distributions. In these simulated shocks both ion species are decelerated differently due to their different charge-mass ratios when they cross the electrostatic shock potential, producing the formation of a ring-beam distribution of He^{++} downstream of the shock [*Fuselier & Schmidt*, 1997; *Lu & Wang*, 2006]. This He^{++} ring-beam distribution can drive helium cyclotron waves, which then scatter He^{++} into a shell-like distribution [*Lu & Wang*, 2006; *Hao et al.*, 2014]. Geotail spacecraft recent observations have made it possible to identify stable He^{++} ring beams in velocity space perpendicular to the magnetic field generated during a bow shock crossing [*Tsubouchi et al.*, 2016].

In the context of interplanetary shocks a recent work [*Ofman et al.*, 2019] compares the observed magnetic and density structure of different oblique shocks at 1 AU with 2D hybrid simulations to demonstrate the effects of He^{++} on the magnetic and density profiles, the dynamics of the downstream shock oscillations as well as the nonstationarity of the shocks.

Given the presence of He^{++} in the solar wind, in this work we investigate its influence on different interplanetary shock signatures performing a group of 2D hybrid simulations of collisionless shocks [*Winske & Leroy*, 1985; *Burgess*, 1987b; *Krauss-Varban*, 2005]. We use the HYPSI code [*Burgess et al.*, 2015; *Gingell et al.*, 2017; *Trotta & Burgess*, 2019] varying the He^{++} number density fraction (1, 5 and 10%) and shock geometry (θ_{Bn} = 15°, 30°, 50° and 65°) for an intermediate Alfvén Mach number ($M_A \sim 4.4$) similar to IP shocks. In this context observational IP shocks with parameters similar to those presented here can be found in the WIND data set (`http://ipshocks.fi/`) where for instance 48 fast forward IP shocks with Mach numbers ($4 < M_A < 5$) are listed covering $0.46 < \beta < 13.07$ and $8° < \theta_{Bn} < 88°$ as well as in past investigations [*Blanco-Cano et al.*, 2016] and recent case-study works [*Enriquez-Rivera et al.*, 2013; *Ofman et al.*, 2019] where observational He^{++} content is similar to the values in our study. This work is organized as follows: In Section 2, we describe the hybrid simulation model and setup, the simulation results are presented in Section 3, and in Section 4 we discuss and summarize our results.

2 Simulation setup

We performed 2D hybrid simulations to investigate the influence of He^{++} on shock dynamics and particle thermalization for different θ_{Bn} initial values and different number content of He^{++} particles. The two dimensional simulations were performed using the hybrid Particle-In-Cell (PIC) code HYPSI [*Burgess et al.*, 2015; *Sundberg et al.*, 2016], that is based on the CAM-CL (see [*Matthews*, 1994] for details) algorithm. Under this approach protons and He^{++} particles are treated kinetically and advanced using the standard PIC method. Electrons are considered as a charge-neutralizing massless fluid [see A.3 in *Burgess & Scholer*, 2015]. Electron inertial and kinetic effects are assumed to be negligible.

Spatial and temporal scales in the simulation are expressed in units of proton inertial length $d_i = c/\omega_p$ (where ω_p is the proton plasma frecuency and c is the speed of light) and Ω_p^{-1} (where Ω_p is the proton gyro frequency) respectively and velocity is normalized to the simulation Alfvén speed $V_A = B_u/\sqrt{\mu_o n_p m_p}$ that does not change with He^{++} fraction. The proton density $n_p m_p$ and magnetic field B_u used to calculate these parameters are also normalized to the initial upstream values. The number of grid cells for all the runs is $n_x \times n_y = 1000 \times 800$ having cell sizes $\Delta x = \Delta y = 0.5\ c/\omega_p$ with velocity, magnetic field, and electric field vectors including all three-dimensional components. The time step Δt was chosen so that $\Omega_p\,\Delta t = 0.005$. In all cases, the plasma is initialised with an inflow speed V_{in} of 3.3 V_A along the x direction and with the magnetic field in the x-y simulation plane.

The injection method has been used to create and sustain the shock transition. The plasma flows along the x direction at the (super-Alfvénic) speed V_{in}. The right boundary of the simulation acts as a perfectly reflecting wall, and plasma is continuously injected at the left (open) boundary. As a consequence of the interaction between the reflected and injected plasma, a shock is produced, and it propagates in the negative x direction. In the simulation frame, the downstream side of the shock is at rest, and the shock normal is antiparallel to the inflow speed. The simulation is periodic in the y direction.

We perform different runs varying the initial angle between the upstream B-field direction and the x-axis (15°, 30°, 50° and 65°) which also corresponds to the nominal angle θ_{Bn} of the shocks. Alpha particles are included in the simulations self-consistently. For each θ_{Bn} value we vary the relative number density fraction of He^{++} i.e. n_α/n_p = 0.01, 0.05, 0.10, with n_α and n_p being the number density fraction of He^{++} and protons respectively. We thus perform 12 simulation runs (see Figure 1).

A finite resistivity, $\eta = 0.06\ \omega_p^{-1}$ is used in the simulations with the upstream ion populations having an isotropic Maxwellian VDF, with an upstream $\beta = 0.5$. In order to keep the statistical noise typical of PIC simulations to a minimum, the number of particles per cell for all the simulations is $\sim$ 100 per species (upstream). This is done to correctly model minor species, even if its fraction is small. It should be noted that the different values of θ_{Bn} for each simulation results in slightly different shocks velocities [*Caprioli & Spitkovsky*, 2014] in the simulation frame (and therefore slightly different M_A) depending on the θ_{Bn} value. We study the shocks once they have reached the same x position (i.e. $x \sim 250\ d_i$) in the middle of the box hence due to different shock velocities, the simulation times of the shocks will differ.

3 Simulation results

3.1 Magnetic field

Figure 1 shows the time evolution of the average magnetic field profile obtained by averaging in the y-direction. In the figure the shock θ_{Bn} values increase from left to right from 15°, 30°, 50° to 65°. The He^{++} number density fraction increases from 1% (top panel), 5% (middle) to 10% (bottom).

The color scale has the same range (from 1 to 3.5) in all plots. The shock can be identified by the abrupt jump in the magnetic field magnitude by a factor of $\gtrsim 2$, with the color changing from blue to red. Although the inflow velocity is the same for all the runs, due to the different θ_{Bn} values the shock velocity and thereby the Alfvénic Mach number vary, being higher as the θ_{Bn} increases: M_A = 4.2, 4.3, 4.5, 4.8 for θ_{Bn} = 15°, 30°, 50° and 65° respectively. The He^{++} number density fraction does not seem to influence the Mach number in a significant manner.

Clear differences can be observed in the averaged magnetic field profile time evolution as θ_{Bn} increases. For the 15° case the magnetic field magnitude exhibits maximum values $\lesssim 3$ in the downstream region (red color) within 25 d_i from shock transition. The width of this plateau tends to increase as the He^{++} number density fraction increases. Further downstream the magnetic field magnitude decreases to $\sim$ 1.5.

In the upstream region the magnetic field fluctuations exhibit amplitudes up to 1.5 near the shock. These upstream fluctuations start to form at the beginning of the simulations very close to the shock, reaching larger distances from the shock as the simulation evolves.

Although not shown here (See Figure S1 in the Supporting Information), the plots of magnetic field magnitude for an horizontal cut in the simulation box at different consecutive times show different compressive waves and whistler wave packets formed upstream of the shock. These waves convect into the shock causing the shock transition to change from a gradual to an abrupt profile contributing to the reformation of the shock as suggested in past works [*Burgess*, 1989a; *Hao et al.*, 2017]. These waves have different characteristics depending on the content of He^{++} particles and will be studied in the future.

In the 30° case the magnetic field magnitude reaches similar maximum values in the downstream region as in the 15° case (< 3) but B values do not decrease as much further downstream, settling at $\sim$ 2. The upstream fluctuations tend to have smaller amplitudes than in the 15° case. They do however behave similarly in the sense that in the beginning they form close to the shock and extend to larger distances from it as the simulation evolves.

For the 50° geometry, the downstream B-field magnitude reaches values of $\lesssim 3$ and there is no clear decrease with distance from the shock in the downstream region. The compressive magnetic fluctuations in the upstream side exhibit considerably smaller amplitudes compared with the previous geometries and begin to appear later in the simulations, after t $\sim 100\ \Omega^{-1}$. Their upstream extensions are much smaller. These upstream increased B-field fluctuations appear later in time as the He^{++} number density fraction increases The onset times are approximately 100, 125 and 170 Ω_p^{-1} for 1, 5 and 10 % of He^{++} respectively. Downstream magnetic field fluctuations decrease their amplitude considerably compared with the less oblique cases and almost no differences are observed in the magnetic signature as the He^{++} percentage changes in the simulations (see also Figure 2).

For the 65° case there are no compressive fluctuations in the upstream region. The shock transition is very abrupt and the B-field increases to values up to ~ 4. A very narrow overshoot is formed immediately behind the shock ramp (see Figure 2) and is followed by a fast decrease to a constant value of ~ 3. The downstream fluctuations for this case have amplitudes similar to those in the 50° case.

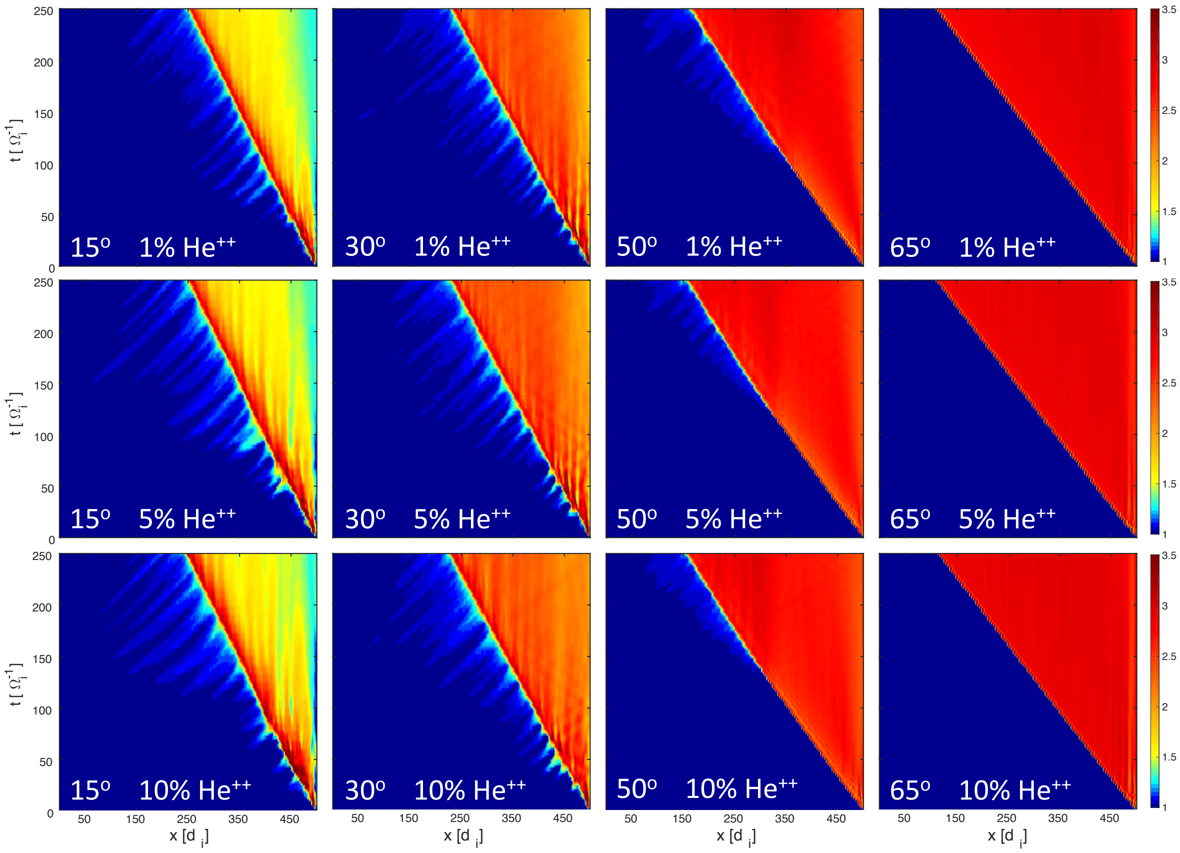

Figure 1. Figure matrix showing the time evolution of total magnetic field (averaged over y-axis) for all the runs in this work. θ_{Bn} increases from left to right while the He^{++} number density fraction increases from top to bottom. The change in color from navy to aqua occurs at ~1.25 while the change from green to yellow occurs at ~ 1.5.

Figure 2 shows the average total magnetic field profiles for all the θ_{Bn} values at the time when the shock arrives to ~ 250 d_i. This time has been chosen based on Figure 1 and corresponds to the time when the upstream waves have properly formed. The three profiles plotted in each panel correspond to different He^{++} number density fractions (black: 1%, red: 5%, blue: 10%).

Figure 2 exhibits clear variations of the averaged shock magnetic field profile. Well developed compressive B-field variations in the upstream region can be identified decreasing in amplitude as θ_{Bn} increases except for the 65° geometry where they do not develop. These variations extend farther upstream for the 15° and 30° cases. The averaged shock front becomes steeper as the shock becomes more oblique. As the θ_{Bn} increases, the shock profile changes from a peak-like to a step-like signature. When θ_{Bn} =65° a sharp overshoot forms just behind the shock followed by an undershoot. For the quasi-parallel cases (θ_{Bn} =15° and 30°) the magnetic field fluctuations after the shock decrease more gradually as the content of He^{++} particles increases. The downstream fluctuations tend to have smaller amplitudes as the θ_{Bn} increases. For the more oblique case (θ_{Bn} = 65°) downstream quasi-periodic fluctuations after the undershoot can be observed growing in amplitude as the content of He^{++} particles increases in agreement with a similar recent work [*Ofman et al.*, 2019] where simulations of shocks with θ_{Bn} = 60° and different percentages of He^{++} are performed and compared with DSCOVR observations. After ~ 350 d_i the downstream compressive fluctuations have almost disappeared, regardless of the He^{++} content. The asymptotic downstream B value is larger as the shock geometry becomes more oblique going from a magnitude of 1.5 for θ_{Bn} =15° to 3 for θ_{Bn} =65° as expected from the fluid shock conservation (Rankie-Hugoniot) relations.

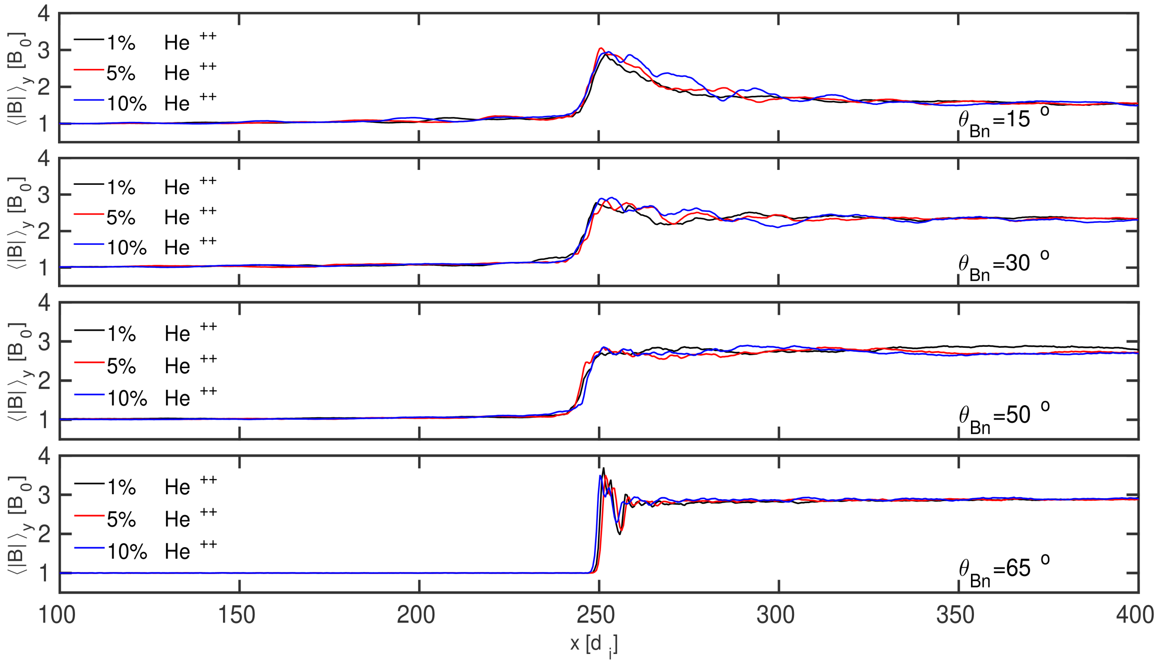

Figure 2. Total magnetic field profile (average over y-axis) for the all the different θ_{Bn} values used in this work when the shock arrives to ~ 250 d_i. The θ_{Bn} angle increases from top to bottom, He^{++} number density fraction is indicated by different colors (black: 1%, red: 5%, blue: 10%).

3.2 Temperature anisotropy

Figure 3 shows the time evolution of proton temperature anisotropy $A_p = (T_\perp/T_\parallel)_p$ averaged over the y-axis for each of our simulations following the same procedure as in Figure 1. The parallel and perpendicular temperatures are calculated from the second velocity moment of the distribution function [see for example *Gary*, 1993] in each cell. The color bar palette was divided in two colors: dark to aqua-blue color to represent the anisotropy values less than one and yellow to red color for anisotropy values from one to two. Figure 3 shows that there are three types of behavior for A_p which are correlated with shock geometry as follows:

• In the case of quasi-parallel shocks with θ_{Bn} = 15° and 30° the upstream region that is filled initially with an isotropic flux ($T_\parallel \sim T_\perp$) starts to be permeated by backstreaming particles coming from the shock leading to $T_\parallel > T_\perp$ as can be observed in dark blue color. As the simulation evolves and more backstreaming particles interact with the incoming plasma near the shock, upstream regions with $A_p > 1$ begin to develop as a consequence of fluctuations in magnetic field which can be corroborated by examining Figure 1. For θ_{Bn} =15° these upstream regions where A_p > 1 seem more fragmented, also their extension to the upstream side is smaller for the case with 1% of He^{++} in comparison with those with higher He^{++} number density fraction. This behavior is also observed for the θ_{Bn} = 30° case being less fragmented in comparison to the less oblique case. The downstream region for both quasi-parallel cases has $A_p \sim 1$ throughout all the simulation, for the θ_{Bn} = 30° case. Small zones with $A_p > 1$ in the immediate downstream region can be observed at early times in the simulations, being less extended for the case with higher He^{++} number density fraction.

• In the case of the oblique shock with θ_{Bn} = 50° a well defined region with $A_p > 1$ develops very early in the simulation just downstream of the shock, appearing closer to it, being larger in extension as the percentage of He^{++} particles increases. A narrow high anisotropy layer with $A_p \sim 2$ is located exactly at the shock transition reducing its magnitude before upstream regions near the shock with $A_p > 1$ start to appear extending more and more towards the upstream side as the simulation evolves. As for the quasi-parallel cases, the upstream region where the incident plasma flow initially has an isotropic distribution start to be permeated by zones with $T_\| > T_\perp$ (dark blue) due to backstreaming particles aligned to the magnetic field lines. As the simulation continues to evolve upstream regions with $A_p > 1$ appear in the upstream region coinciding with zones with compressive magnetic field fluctuations as discussed in Figure 1. These upstream regions where $A_p > 1$ appear at earlier times ($t < 150\Omega_i^{-1}$) for the simulation with 1% of He^{++} particles in comparison with the 10% case ($t > 150\Omega_i^{-1}$). The upstream transition region from $T_\| \sim T_\perp$ to $T_\| > T_\perp$ is not as sharp as in the quasi parallel cases and the extent of this region lasts longer since the regions with $A_p > 1$ begin to develop at more advanced times for this geometry. Also the region with $T_\| > T_\perp$ appears in the upstream region later in time (t > 100 Ω_i^{-1}) in comparison with its quasi parallel counterpart (t ∼ 100 Ω_i^{-1}) which is in agreement with the less efficient parallel transport of particles expected for this quasi-perpendicular geometry. In contrast to the other geometries, for this case the different behavior in the immediate upstream side of the shock after $t \sim 150\ \Omega^{-1}$ when upstream B-field fluctuations starts to develop allowing the increase in temperature anisotropy that define a characteristic simulation time associated with growth and convection of upstream fluctuations that could not be observed if the simulation had not lasted so long. It must also be mentioned that the "wall effect" observed near the right wall is not physical but a falsely perceived effect due to the high contrast colors near $A_p \sim 1$.

• In the case of the shock with θ_{Bn} = 65° the value of A_p is greater than one through all the downstream region reaching the maximum value (> 8) in the region adjacent to the shock transition during the whole time of the simulation. The proton anisotropy value is ∼ 1 throughout all the upstream region in agreement with the fact that the rate of backstreaming particles is almost null for this high θ_{Bn} case and no upstream magnetic field fluctuations are present in Figure 1.

Figure 4 shows semi-log plots of $T_\perp/T_\|$ (averaged over y-axis) for protons (blue) and He^{++} (orange) at the time when the shocks arrive to ∼ 250 d_i. The shock position is marked with a vertical dashed line while the horizontal dashed line indicates $T_\perp/T_\| = 1$. For clarity only a range from 100 d_i to 300 d_i in the x-axis and from 0.5 to 5 (with minor ticks spaced each 0.25) in the y-axis are plotted. As before, the temperature anisotropy profiles show three distinct behaviors:

• Quasi parallel cases (θ_{Bn} = 15°, 30°): For both geometries the upstream value of $A_p \sim 0.75$ at x=100 d_i increases to values $\gtrsim 1$ in some x-intervals near the shock region that are more extended and reach higher values as the He^{++} number density fraction increases. In general A_p is greater than the He^{++} temperature anisotropy $A_\alpha = (T_\perp/T_\|)_\alpha$ in the upstream region. In the downstream region A_p exhibits a decrement to values less than 1 while A_α rises sharply reaching a maximum peak value (∼ 1.5 for 15° and ∼ 1.75 for 30°) at the shock transition to then decrease to ∼ 1. For the case with θ_{Bn} = 30° the A_α peak at the shock transition tends to be wider as the He^{++} percentages increase.

• Oblique case (θ_{Bn} = 50°) : In contrast to the quasi parallel geometries, here A_p at x =100 d_i becomes increasingly smaller as the He^{++} content grows. x-intervals with $A_p > 1$ that are less extended and reach lower values as the He^{++} number density fraction increases can be observed. Then A_p drops significantly in the upstream region adjacent to the shock. This drop is less pronounced in the case of the 10 % He^{++} run. Unlike for the quasi parallel cases, for this geometry $A_p < A_\alpha$ along

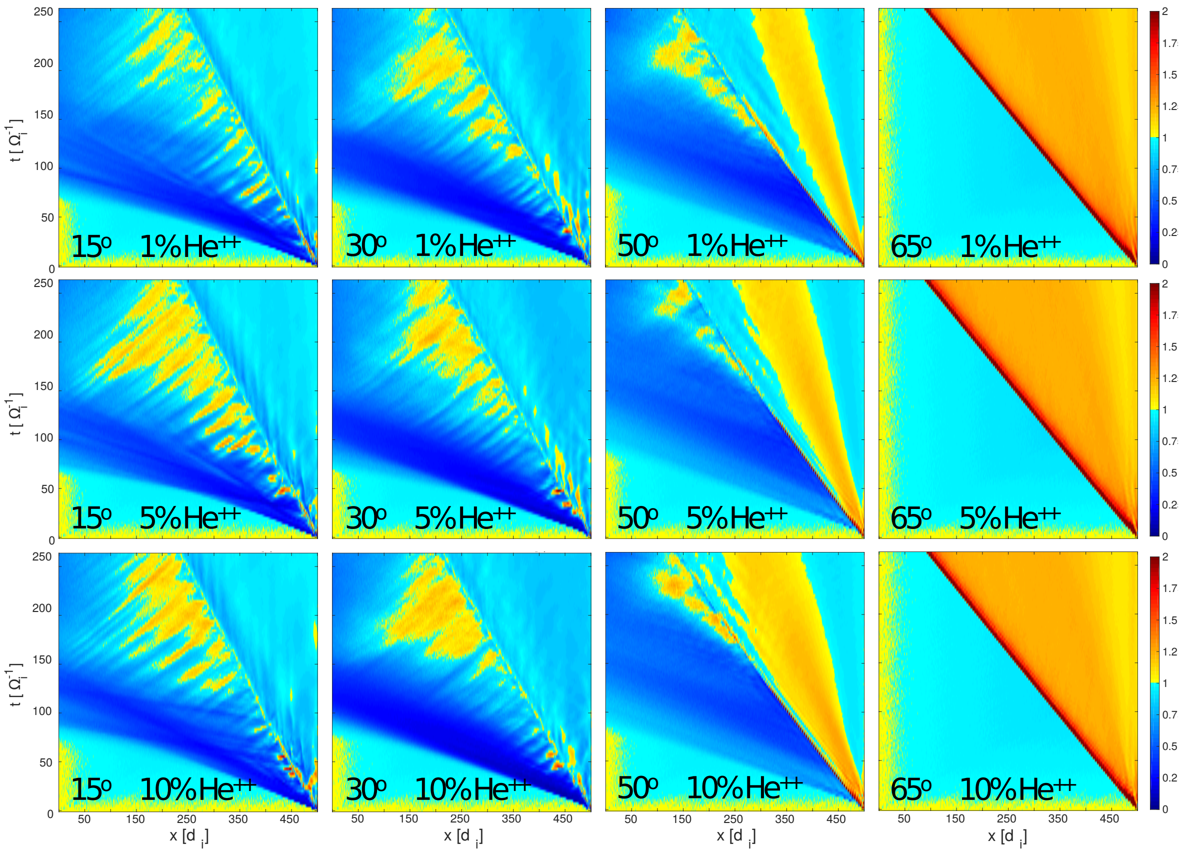

Figure 3. Figure matrix showing the time evolution of temperature anisotropy for protons (averaged over y-axis) for all the runs in this work. θ_{Bn} increases from left to right while the He^{++} number density fraction increases from top to bottom. The color palette is chosen to show anisotropy values less (in blue) and greater (in yellow-red) than 1.

all the upstream side except for the 1 % He^{++} case where a region with $A_p \sim A_\alpha$ at about $x \sim 200$ d_i can be observed. Downstream of the shock A_p decreases to values less than one. The value of A_α rise sharply reaching a peak at the shock transition that increases in value (2.75, 3.75, 4.25) as the He^{++} percentage does and then drops in the downstream region. This fall becomes more abrupt, making the width of the peak thinner as the content of He^{++} particles increases.

- Quasi-perpendicular geometry (θ_{Bn} = 65°): Here the value of A_α is 1 throughout all the upstream region, then rises sharply at the shock transition reaching smaller peak values (8.2, 7.8, 7.5) as the He^{++} number density fraction increases, and then decreasing in the downstream region. This drop is not monotonic since downstream oscillations of A_α can be observed as a consequence of the coherent gyration of He^{++} particles as pointed in previous works [*McKean et al.*, 1996; *Hao et al.*, 2014] and discussed here in section 3.3. For protons, the upstream values of A_p are just below 1, then increase substantially at the shock transition to values that are, in contrast to A_α, greater (8.8, 8.9, 9.31) as the He^{++} content increases. Then A_α drop to $\sim$ 1.25 in the downstream region. The decrease here does not show downstream oscillations which can be explained in terms of the differences in charge to mass ratios for both species.

Additionally, we performed an extra simulation (not shown) with θ_{Bn} = 75° in order to see if there are differences comparing with the θ_{Bn} = 65° case. We did not find significant changes beyond the expected increment in the downstream overshoot magnitude.

3.3 Velocity distribution functions

We also investigate the behavior of the velocity distribution functions (VDFs) for both ion species in the shock interface zone along the shock surface as well as at different x coordinates for the time when the shock is at x=250 d_i. We show four cases corresponding to θ_{Bn} = 15°, 65° with 1 and 10% of He^{++} since they exemplify the main VDF characteristics due to variations in the angle θ_{Bn} from quasi-parallel to quasi-perpendicular and the low and high number density fraction in He^{++} particles. It is important to mention that the number density of points in VDFs depends on the number of particles per cell so that the relative fraction of He^{++} to protons is not seen when comparing VDFs for the two species.

Figure 5 displays the cases for θ_{Bn} = 15° with 1% and 10% of He^{++}. By comparing Figures 5a and 5c we can observe that the downstream region exhibits higher amplitude magnetic fluctuations reaching values (> 3) along a larger range of x in the case of the shock with 10% of He^{++}. In panels 5b and 5d where cuts along y=100 d_i (red) and y=250 d_i (blue) are shown, variations in downstream magnetic field are clearly observed. In addition, for the 10% case the variations between both cuts along y-direction are more pronounced compared to the case with lower He^{++} number density fraction. Upstream of the shock whistler precursors are observed in both He^{++} cases for the bottom cut (in red) due to the irregular shock front profile. Whistlers are not found in the top cut (in blue).

Figures 5e and 5f show the upstream and downstream VDFs respectively for both species in the regions inside the magenta boxes in Figure 5c corresponding to the case with 10% of He^{++} particles. The proton VDF in the upstream region (V_x-V_y space) has two principal components (Figure 5e): A main beam centered at (V_x, V_y, V_z) = (3.3, 0, 0) V_A corresponding to the inflow particles and a secondary component of backstreaming particles (V_x < 3.3). Comparing the upstream VDFs of both species we notice that the secondary component of the VDF corresponding to protons is more populated and reaches higher values in velocity than its He^{++} counterpart.

Although they are qualitatively similar, the differences between VDFs at different vertical locations in the upstream side (not showed) can be attributed to the deformation of the shock front which produces different local geometry (Figures 5a and 5c) that leads to different plasma processing along the shock and inside the collecting boxes as can be corroborated by observing the differences in magnetic profiles in panels 5b and 5d for regions on both sides of the shock.

For the downstream side (Figure 5f) the thermalization of particles through the shock potential produces a spread of the VDF for both species in all directions. Again, the VDF in V_x-V_y space tends to be more isotropic ($T_\perp/T_\parallel \sim 1$) for protons than for alphas (Figure 5f) which is in agreement with Figure 4. As for the upstream side, there are differences in the VDF's at different y-coordinates in the downstream side but they are not so pronounced, and this can be explained in terms of the differences in the turbulent magnetosheath region as can be observed for both profiles in magnetic field in Figure 5d.

Figure 6 shows the θ_{Bn} = 65° simulation with 1 and 10% of He^{++} particles in the same format as Figure 5. As in the previous case Figures 6a and 6c show that the downstream region is permeated by larger amplitude field fluctuations when the number density fraction of He^{++} is higher. This behavior is corroborated comparing Figures 6b and 6d where the profiles show more turbulence in magnetic field for the case with 10% of He^{++}. Also the differences in magnetic field profiles are more pronounced for the case with the highest percentage of helium He^{++}. For the upstream side no differences between cases with different He^{++} percentage are found for the magnetic field. In contrast to the quasi parallel cases, here the shock transition is sharp and presents a clear overshoot.

Figure 6e for the θ_{Bn} = 65° shows clearly less particles for both species in the upstream side in comparison with the θ_{Bn} = 15° case in Figure 5. The VDF only shows some of the reflected-gyrating ions which will eventually end up in the downstream region. In addition, for this case very few backstreaming He^{++} particles can be observed when comparing with protons (lower panels in 6e). This can be explained by the differences of mass for both species that facilitates protons to be more efficiently reflected to the upstream side than their He^{++} counterpart as reported in previous simulation works (See for example [*Burgess*, 1989b]) and in agreement with [*Broll et al.*, 2018] where data and hybrid simulations of a bow shock observed by the Magnetospheric Multiscale (MMS) mission indicate that the amount of He^{++} that reflects at the shock is smaller than the proton population.

Figure 6f shows different behaviors for proton and He^{++} particles in the downstream region. He^{++} particles tend to form a ring-like distribution centered in (V_x, V_z) = (0, 0) in agreement with previous works such as [*Hao et al.*, 2014], who explain this ring as a consequence of differentially deceleration of He^{++} particles compared to protons due to their different charge-to-mass ratio as they cross the shock potential. On V_x-V_y panels in Figure 6f it is possible to see that both species differ mainly in the width of their distributions functions along V_x as expected from the results from Figure 4 where the anisotropy value has a broader and higher peak in the immediate downstream region for He^{++} particles than for protons. Because of the quasi-perpendicular geometry for this case, there are no pronounced irregularities along the shock front as can be observed in Figure 6b and Figure 6d in contrast with the θ_{Bn} = 15° case (panels b and d in Figure 5). Although not showed here (see Figure S2 in the Supporting Information) when compared VDFs between different He^{++} percentages for this quasi perpendicular case it can be observed that the downstream VDFs for both species tend to be more diffuse for the case with higher He^{++} percentage, this can be explained as a consequence of the more perturbed magnetic field on the downstream side of the shock as the He^{++} number density fraction increases as can be observed from the differences between horizontal cuts for both He^{++} cases here (Figures 6b and 6d).

The characteristics of VDFs found here are in agreement with previous works [*Motschmann & Glassmeier*, 1993] that is, whereas in quasi-parallel configurations the scattering of protons in V_x-V_y space is rather isotropic (Figure 5f) in the quasi-perpendicular case it remains anisotropic (Figure 6f). In the last case the He^{++} distribution in V_x-V_z space is a ring around the magnetic field vector mainly pointed in y direction (Figure 6f).

Figure 7 shows the densities of protons and He^{++} particles corresponding to the same simulations and times as in Figures 5 and 6. Clear differences can be observed when comparing both geometries. While for the quasi-parallel case (panels a and b) the shock interface is not well defined and presents the typical rippling as well as not coherent fluctuations at both sides of the shock, for the quasi-perpendicular shock (panels c and d) the shock interface is well defined, no upstream density structures can be observed and a wave-like structure is evident behind the shock decreasing in amplitude further in the downstream region. When we analyze the differences for the same geometries taking in account the He^{++} content in the simulations the effect is more evident for the quasi-perpendicular case (panels c and d) where the fluctuations are more defined but with lower amplitudes for the cases with less He^{++} content. This feature is correlated with both the temperature anisotropy and the magnetic field magnitude in the same regions as can be corroborated in Figures 4, 5 and 6. This is in agreement with [*Ofman et al.*, 2019] who explain this behavior in terms of the He^{++} "surfing" [*Lee et al.*, 1996] along the shock front evidenced by the strong localized density peaks.

3.4 Mirror and ion/cyclotron instability analysis

In this section we study the growing of mirror and ion/cyclotron waves [*Gary*, 1993] using instability thresholds related with temperature anisotropy and plasma beta parameters in order to know when these modes can grow. This analysis is valid for cases where the condition $T_\perp/T_\parallel > 1$ is well fulfilled for protons [*Gary*, 1993; *McKean et al.*, 1995a,b] namely in the downstream region for our θ_{Bn} = 65° cases as can be corroborated in Figure 4 and Figure 6f where the downstream VDFs are shown. For this purpose in Figure 8 some cuts of proton anisotropy ($T_\perp/T_\parallel$) and magnetic field at $y = 200\ d_i$ and just behind the shock corresponding to the same simulation times of those in Figure 7c,d are shown. In addition to $T_\perp/T_\parallel$ the parameters $\mathrm{M} = 1 + 1/\beta_\perp$ (in red) and $\mathrm{IC} = 1 + \beta_\parallel^{0.5}$ (in blue) are shown in the same panel. From these it follows that the growing threshold of mirror instability is fulfilled when $T_\perp/T_\parallel > \mathrm{M}$ [*Southwood and Kivelson*, 1993] while the corresponding condition for the ion/cyclotron instability approximate threshold is $T_\perp/T_\parallel < \mathrm{IC}$ [*Gary et al.*, 1996; *Anderson et al.*, 1996]. As can be observed in Figure 8 for both He^{++} concentrations simulations the ion/cyclotron threshold is fulfilled along the cut. For the mirror instability the threshold is barely fulfilled only at some located intervals near the shock interface. These results are in agreement with [*McKean et al.*, 1995a,b; *Hao et al.*, 2014] who studied with hybrid simulation quasi-perpendicular shocks with similar parameters finding that ion/cyclotron waves can grow in the downstream region by the energy provided by the ion temperature anisotropy. Not many differences are observed when comparing the results for both He^{++} relative abundances except for an increase in the size of the regions where the mirror instability threshold is met for the 10% He^{++} case which leads to a reduction in the size of regions near the shock where the ion/cyclotron threshold is fulfilled. These results could be improved with a full kinetic instability calculation in a future work.

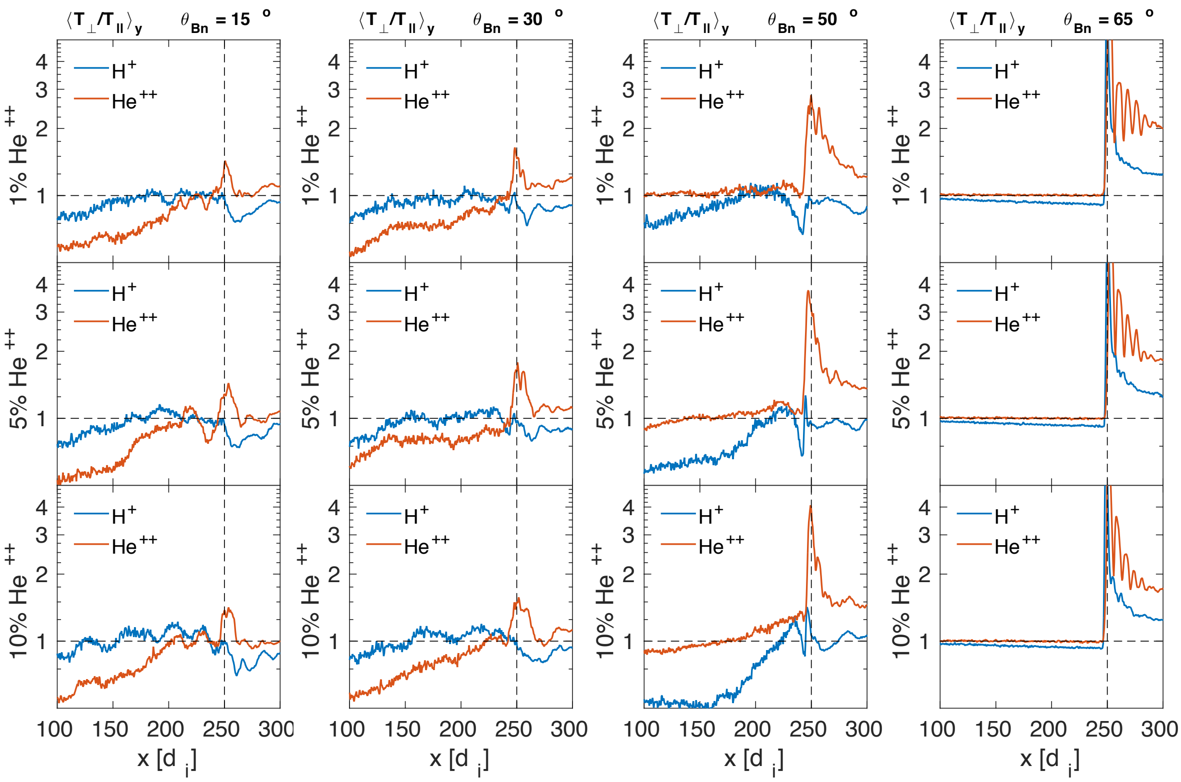

Figure 4. Semi-log temperature anisotropy profiles (average over y-axis) for protons (blue) and He^{++} (orange) at the time when the shock arrives to $\sim 250\ d_i$ for all the θ_{Bn} values and He^{++} percentages in this work. The vertical dashed line indicates the shock localization and the horizontal dashed line indicates $T_\perp/T_\parallel = 1$

4 Discussion and Conclusions

Although the dependence of shock dynamics, temperature anisotropy and VDF evolution with shock geometry (θ_{Bn}) has been widely studied in the past with the help of both, observations and computer simulations, the influence of He^{++} number density fraction on interplanetary shock enviroments has received less attention. In order to study this influence we have analyzed the results of twelve 2D local hybrid simulations of quasi-parallel (θ_{Bn} = 15°, 30°) and quasi-perpendicular (θ_{Bn} = 50°, 65°) collisionless shocks varying the number density fraction of He^{++} particles (1%, 5%, 10%). Our study shows that both the geometry and the content of He^{++} particles can modify the interplanetary shock profile and the characteristics of the upstream and downstream regions affecting temperature anisotropy, VDF properties and magnetic fluctuations growth.

The variation of initial θ_{Bn} changes the efficiency with which particles can escape to the upstream side of the shock influencing the formation of compressive structures in the magnetic field profile. Quasi-parallel geometries (θ_{Bn} = 15°, 30°) allow particles to be transported efficiently farther in the upstream region along the magnetic field lines. The interaction between these backstreaming particles and the incoming plasma flow results in upstream magnetic field fluctuations. The upstream variations of the averaged B-field profiles tend to have larger amplitudes and extend further to the upstream region for the 15° case. The shock with oblique geometry (θ_{Bn} = 50°) takes more time to develop these fluctuations and these reach lower amplitudes and extend less towards the upstream region compared with quasi-parallel cases. For the quasi-perpendicular shock (θ_{Bn} = 65°) no upstream magnetic field fluctuations form. In the downstream region such fluctuations tend to decrease in amplitude and length as the θ_{Bn} increase.

The magnetic field profile is also affected by shock geometry. The expected increment of magnetic field in the shock interface tends to be more abrupt as the θ_{Bn} increases. For the quasi-parallel geometries (θ_{Bn} = 15°, 30°) the magnetic field magnitude decreases in the downstream side from the shock jump, this decrement is more gradual for the θ_{Bn}= 30° case. In contrast, for the oblique geometry (θ_{Bn} = 50°) the magnetic field profile has a step-like shape. For the quasi-perpendicular geometry (θ_{Bn} = 65°) the same step-like profile is observed with a clear overshoot just after the shock jump followed by a decrement in magnetic field to an almost constant downstream side value.

The temperature anisotropy for protons (A_p) is also affected by θ_{Bn}. For the quasi-parallel cases (θ_{Bn}= 15° and 30°) the upstream side starts to be permeated by backstreaming particles since the beginning of the simulation which produce regions with $T_\parallel > T_\perp$. As the simulation evolves and backstreaming particles interact with the incoming plasma, upstream regions with $A_p > 1$ start to appear due to the fluctuations in magnetic field which can heat and scatter the particles in the perpendicular direction to the magnetic field. For the oblique case (θ_{Bn}= 50°) the upstream zones where A_p> 1 are less extended and appear later in time in comparison to the quasi-parallel cases, which is due to the fact that backstreaming particles are less efficiently transported to the upstream region far from the shock as the geometry becomes more oblique. In the quasi-perpendicular shock with θ_{Bn}= 65° there are no zones where A_p >1 in the upstream side which can be explained in terms of the so oblique geometry that does not allow particles to escape beyond the foot-ramp region. In the downstream region $A_p \sim 1$ for the quasi-parallel cases (θ_{Bn}= 15° and 30°), for the oblique geometry (θ_{Bn} = 50°) a zone with A_p> 1 appears, with a size that growths as the simulation evolves. For the quasi-perpendicular shock with θ_{Bn}= 65° the perpendicular temperature presents a sudden increase in the shock transition due to the gyration of reflected particles that are convected into the downstream region increasing its perpendicular velocity. Then they suffer a rapid isotropization in the region downstream of the overshoot that are associated with the fluctuations present in the downstream region. These then diminish in amplitude with increasing distance downstream of the shock as has been observationally reported by [*Sckopke et al.*, 1990].

The temperature anisotropy for both species (A_p, A_α) also shows a dependency on θ_{Bn}. For the quasi-parallel cases (θ_{Bn}= 15° and 30°) $A_\alpha < A_p$ in the upstream region and $A_\alpha > A_p$ in the downstream region. For the oblique geometry (θ_{Bn}= 50°) $A_\alpha > A_p$ in general along all the simulation box. In the quasi-perpendicular shock (θ_{Bn}= 65°) $A_\alpha \sim A_p \sim 1$ in the upstream region and then increase suddenly at the shock, decreasing in the downstream region with $A_\alpha > A_p$ and a fluctuating pattern for the He^{++} component. For all the geometries a peak ($A_\alpha > 1$) is formed at shock transition that tends to be larger as the value of θ_{Bn} increases.

The VDFs for both species are also affected by θ_{Bn}. For the θ_{Bn}= 15° case backstreaming particles of both species can be observed in the immediate upstream region in contrast to the quasi-perpendicular case (θ_{Bn} = 65°) where the percentage of particles that do not belong to the inflow beam is much smaller. In contrast to the proton distributions, a ring-like distribution is formed in the immediate downstream side for He^{++} particles as a consequence of differential acceleration due to the different charge to mass ratio of both species. Also the downstream VDFs for protons are more isotropic and thermalized for the θ_{Bn}= 15° case than for the θ_{Bn}= 65° case.

We find that the content of He^{++} also slightly affects the magnetic field structure at both sides of the shock. In quasi-parallel shocks (θ_{Bn} = 15°, 30°) the compressive magnetic fluctuations on both sides of the shock tend to reach higher amplitudes for the cases with more He^{++} content. In contrast, for the shock with θ_{Bn}= 50° the increment in He^{++} number density fraction does not seem to affect the amplitude of these fluctuations. Although for the quasi-perpendicular case with θ_{Bn}= 65° no upstream compressive fluctuations are observed, in the downstream side these fluctuations tend to reach larger amplitudes for the cases with more He^{++} content due to the increase of the temperature anisotropy in the immediate downstream region as the percentage of He^{++} particles increases (as will be discussed below).

The temperature anisotropy for protons (A_p) is also affected by the He^{++} content: The upstream zones where $A_p > 1$ coincide with those where compressive magnetic fluctuations are present as expected because fluctuations in magnetic field can produce heating and scattering of particles in the perpendicular direction relative to the magnetic field. For the quasi-parallel cases (θ_{Bn}= 15° and 30°) the upstream zones where $A_p > 1$ are less fragmented for the simulations where the number density fraction of He^{++} is higher. For the oblique case (θ_{Bn}= 50°) this behavior is repeated while for the downstream region the zone with $A_p > 1$ is closer to the shock zone for the case where the He^{++} number density fraction is larger. When comparing the temperature anisotropy for both species (A_p, A_α) we can observe that although the content of He^{++} particles does not affect significantly the shape of the peak at the shock transition for the quasi-parallel cases, for the oblique case (θ_{Bn}= 50°) a clear increment is observed as the number density fraction of He^{++} increases and for the quasi-perpendicular simulations (θ_{Bn}= 65°) the opposite happens, the peak decreases as the number density fraction of He^{++} increases.

The fact that for all our simulations, except in the more oblique case (θ_{Bn}= 65°), upstream zones where $T_\perp > T_\parallel$ coincide with those where compressive magnetic field fluctuations are present is in agreement with recent results of [*Gingell et al.*, 2017] where MMS observations show $T_\perp > T_\parallel$ in the upstream side of a marginally quasi-parallel bow shock ($\theta_{Bn} \sim 45°$) in regions where compressive fluctuations in the magnetic field occur.

The percentage of He^{++} particles also affects the VDF distributions making them more spread as the percentage of He^{++} increases in both quasi-parallel and quasi-perpendicular cases. This is a consequence of the enhanced fluctuations in magnetic field which occur when the He^{++} content is higher.

Finally, the results obtained in this work are relevant for the study of IP shocks driven by coronal mass ejections in the context of Parker Solar Probe and Solar Orbiter missions which will collect data with high resolution at different helio-distances close to the Sun. This will allow us to directly compare our simulation models with observations for shocks at different stages of evolution. Future work include an in-depth analysis on the evolution of waves and kinetic instabilities at and near the shock for both quasi-parallel and quasi-perpendicular cases, shock reformation and physical mechanisms concerning particle reflection and heating as well as VDF behavior through the upstream region to determine the helium foreshock extension.

Acknowledgments
We thank Dirección General de Cómputo y de Tecnologías de Información y Comunicación (DGTIC) of the Universidad Nacional Autónoma de México (UNAM) for the allocation and support received in the use of the HP Cluster Platform 3000SL supercomputer (MIZTLI). Contract grant sponsor: DGTIC-UNAM resources (project LANCAD-UNAM-DGTIC-337). The authors acknowledge support from the Royal Society Newton International Exchange Scheme (Mexico) grant NI150051.

L.P. thanks CONACYT becas nacionales 2015-2019 grant 174700. X. B. C. is supported by CONACyT grant (255203) and DGAPA project (IN105218-3). D. B. was supported by the UK Science and Technology Facilities Council (STFC) grant ST/P000622/1. D.T. acknowledges support of a studentship funded by the Perren Fund of the University of London. P.K. is supported by PAPIIT grant (IA101118). Simulation data used in this research are publicly available at `https://doi.org/10.5281/zenodo.3697360`.

References

Aguilar-Rodriguez, E., Blanco-Cano, X., Russell, C. T. , Luhmann, J. G., Jian, L. K., & Ramirez Velez, J. C. (2011), Dual observations of interplanetary shocks associated with stream interaction regions, J. Geophys. Res., 116, A12109, doi:10.1029/2011JA016559

Anderson, B. J., Denton, R. E., Ho, G., Hamilton, D. C., Fuselier, S. A., Strangeway, R. J. (1996). Observational test of local proton cyclotron instability in the Earth's magnetosphere. Journal of Geophysical Research 101, 21527.

Anderson, B. J., & Fuselier S. A. (1993), Magnetic pulsations from 0.1 to 4.0 Hz and associated plasma properties in the Earth's subsolardepletion magnetosheath and plasma depletion layer,J. Geophys. Res.,98, 1461-1479, doi:10.1029/92JA02197

Blanco-Cano, X., et al. (2016), Interplanetary shocks and foreshocks observed by STEREO during 2007-2010,J. Geophys.Res. Space Physics,121, 992-1008

Blandford, R. D. & Ostriker, J. P. (1978) Particle acceleration by astrophysical shocks. Astrophysical Journal, Part 2 - Letters to the Editor, vol. 221, Apr. 1, 1978, p. L29-L32.

Broll, J. M., Fuselier, S. A., Trattner, K. J., Schwartz, S. J., Burch, J. L., Giles, B. L., & Anderson, B. J. (2018). MMS observation of shock-reflected He^{++} at Earth's quasi-perpendicular bow shock. Geophysical Research Letters, 45, 49-55.

Burgess, D., et al. (2005), Quasi-parallel shock structure and processes, Space Sci. Rev., 118, 205-222.

Burgess, D. (1987a), Shock drift acceleration at low energies. Journal of Geophysical Research, vol. 92, Feb. 1, 1987, p. 1119-1130.

Burgess, D. (1987b), Numerical simulation of collisionless shocks, in Proceedings of International Conference on Collisionless Shocks, Balatonfured, Hungary, edited by K. Szego, pp. 89-111, Central Research Institute for Physics of Hungarian Academy of Sciences, Budapest, 1987

Burgess, D.(1989a) Cyclical behavior at quasi-parallel collisionless shocks. Geophys. Res. Lett. 16, 345-349

Burgess, D.(1989b) Alpha particles in field-aligned beams upstream of the bow shock: Simulations. Geophys. Res. Lett. 16, 163-166

Burgess, D. & Scholer, M. (2015), Collisionless Shocks in Space Plasmas, by David Burgess, Manfred Scholer, Cambridge, UK: Cambridge University Press, 2015

Burgess, D., Hellinger, P., Gingell, I., & Trávnícek, P. M. (2015). Microstructure in two and three-dimensional hybrid simulations of perpendicular collisionless shocks. Journal of Plasma Physics,82, 905820401.

Caprioli, D. & Spitkovsky, A. (2014). Simulations of Ion Acceleration at Non-relativistic Shocks. I. Acceleration Efficiency. The Astrophysical Journal, Volume 783, Issue 2, article id. 91, 17 pp.

Caprioli, D., Yi, D., Spitkovsky, A. (2017). Chemical Enhancements in Shock-Accelerated Particles: Ab initio Simulations. Physical Review Letters, Volume 119, Issue 17, id.171101

Enriquez-Rivera, O., X. Blanco-Cano, C. T., Russell, L. K., Jian, J. G., & Luhmann (2010) Mirror Mode Structures in the Solar Wind: STEREO Observations, AIP Conference Proceedings 1216, 276 (2010); doi: 10.1063/1.3395854

Enriquez-Rivera, O., Blanco-Cano, X., Russell, C. T., Jian, L. K., Luhmann, J. G., Simunac, K. D., & Galvin, A. B. (2013), Mirror-mode storms inside stream interaction regions and in the ambient solar wind: A kinetic study, J. Geophys. Res. Space Physics, 118, 17-28

Fuselier, S. A., & Schmidt, W. K. H. (1994), H^+ and He^{2+} heating at the Earth's bow shock, J. Geophys. Res., 99, 11,539-11,546, doi:10.1029/ 94JA00350

Fuselier, S. A., & Schmidt, W. K. H. (1997), Solar wind He^{2+} ring-beam distributions downstream from the Earth's bow shock, J. Geophys. Res., 102, 11,273-11,280, doi:10.1029/97JA00643

Gary, S. P. (1993), Theory of Space Plasma microinstabiblities. Cambridge University Press.

Gary, S. P., McKean, M. E., & Winske, D. (1996), Proton temperature anisotropy in the magnetosheath: Hybrid simulations, Geophys. Res. Lett., 23, 2887-2890.

Gedalin, M. (2017). Effect of alpha particles on the shock structure. Journal of Geophysical Research: Space Physics,122, 71-76

Geiss, J., Hirt, P., Leutwyler, H. (1970). On Acceleration and Motion of Ions in Corona and Solar Wind. Solar Physics 12, 458.

Gingell et al. (2017), MMS Observations and Hybrid Simulations of Surface Ripples at a Marginally Quasi-Parallel Shock. Journal of Geophysical Research: Space Physics, Volume 122, Issue 11, pp. 11,003-11,017

Gosling, J. T. & Thomsen, M. F. (1985) Specularly reflected ions, shock foot thicknesses, and shock velocity determinations in space. Journal of Geophysical Research, vol. 90, Oct. 1, 1985, p. 9893-9896

Gosling, J. T., Thomsen, M. F., Bame, S. J. & Russell, C. T. (1989) Ion reflection and downstream thermalization at the quasi-parallel bow shock. Journal of Geophysical Research, vol. 94, Aug. 1, 1989, p. 10027-10037

Hada, T., Oonishi, M., Lembége, B., & Savoini, P. (2003), Shock front nonstationarity of supercritical perpendicular shocks, J. Geophys. Res., 108(A16), 1233, doi:10.1029/2002JA009339

Hao, Y., Lu, Q., Gao, X., Huang, C., Lu, S., Shan, L., & Wang, S. (2014), He^{2+} dynamics and ion cyclotron waves in the downstream of quasi-perpendicular shocks: 2-D hybrid simulations, J. Geophys. Res. Space Physics, 119, 3225-3236, doi:10.1002/2013JA019717

Hao, Y., Lu, Q., Gao, X. & Wang, S. (2016), Ion Dynamics at a Rippled Quasi-parallel Shock: 2D Hybrid Simulations, The Astrophysical Journal, Volume 823, Issue 1, article id. 7, 11 pp.

Hao, Y., Gao, X., Lu, Q., Huang, C., Wang, R., & Wang, S. (2017), Reformation of rippled quasi-parallel shocks: 2-D hybrid simulations, J. Geophys. Res. Space Physics, 122, 6385-6396, doi:10.1002/2017JA024234

Ipavich, F. M., Gosling, J. T., Scholer, M. (1984), Correlation between the He/H ratios in upstream particle events and in the solar wind. Journal of Geophysical Research, vol. 89, March 1, 1984, p. 1501-1507.

Kajdič, P., Blanco-Cano, X., Aguilar-Roriguez, E., Russel, C. T., Jian, L. K., & Luhmann, J. G. (2012), Waves upstream and downstream of interplanetary shocks driven by coronal mass ejections, J. Geophys. Res.,117, A06103, doi:10.1029/2011JA017381

Kajdič, P., Preisser, L.; Blanco-Cano, X.; Burgess, D. & Trotta, D. (2019), First Observations of Irregular Surface of Interplanetary Shocks at Ion Scales by Cluster, The Astrophysical Journal Letters, Volume 874, Issue 2, article id. L13, 11 pp.

Kasper, J. C., Stevens, M. L., Lazarus, A. J., Steinberg, J. T., Ogilvie, K. W. (2007). Solar Wind Helium Abundance as a Function of Speed and Heliographic Latitude: Variation through a Solar Cycle. The Astrophysical Journal 660, 901.

Krauss-Varban, D. (2005), From theoretical foundation to invaluable research tool: Modem hybrid simulations, Proceedings of the 7th International Symposium for Space Simulations (ISSS-7), pp. 15-18, Kyoto Univ.,arXiv:physics/0610133

Lee, M. A., Shapiro, V. D., Sagdeev, R. Z. (1996), Pickup ion energization by shock surfing. Journal of Geophysical Research 101, 4777.

Lembège, B., & Savoini, P. (1992), Nonstationarity of a two-dimensional quasiperpendicular supercritical collisionless shock by self-reformation, Phys. Fluids B, 4, 3533-3548, doi:10.1063/1.860361

Lu, Q. M., & Wang, S. (2005), Formation of He^{2+} shell-like distributions downstream of the Earth's bow shock, Geophys. Res. Lett., 32, L03111, doi:10.1029/2004GL021508

Lu, Q. M., & Wang, S. (2006), Electromagnetic waves downstream of quasi-perpendicular shocks, J. Geophys. Res., 111, A05204, doi:10.1029/2005JA011319

Matthews, A. P. (1994), Current Advance Method and Cyclic Leapfrog for 2D Multispecies Hybrid Plasma Simulations, JCoPh, 112, 102

McKean, M. E., Omidi, N., Krauss-Varban, D. & Karimabadi, H. (1995a), Wave and particle evolution downstream of quasi-perpendicular shocks, Adv. Space Res., 15, 319-22.

McKean, M. E., Omidi, N., Krauss-Varban, D. (1995b). Wave and ion evolution downstream of quasi-perpendicular bow shocks. Journal of Geophysical Research 100, 3427.

McKean, M. E., Omidi, N., & Krauss-Varban, D. (1996), Magnetosheath dynamics downstream of low Mach number shocks, J. Geophys. Res., 101, 20,013-20,022, doi:10.1029/96JA01461

Motschmann, U., & Glassmeier, K. (1993). Simulation of heavy ion ring and shell distributions downstream of the bow shock, Geophysical Research Letters, vol. 20, no. 10, p. 987-990.

Neugebauer, M., Snyder, C. W. (1966.) Mariner 2 Observations of the Solar Wind, 1, Average Properties. J. Geophys. Res. 71, 4469.

Ofman, L., Koval, A., Wilson, L., & Szabo, A. (2019). Understanding the Role of α Particles in Oblique Heliospheric Shock Oscillations, J. Geophys. Res. vol. 124, no. 4, p. 2393-2405.

Russell, C. T., & Hoppe, M. (1983), Upstream waves and particles, SSRv,34, 155

Scholer, M., & Burgess, D. (1992), The role of upstream waves in supercritical quasi-parallel shock reformation, J. Geophys. Res., 97,8319-8326, doi:10.1029/92JA00312

Scholer, M., & Terasawa, T. (1990) Ion reflection and dissipation at quasi-parallel collisionless shocks. Geophys. Res. Lett. 17, 119-122. doi:10.1029/GL017i002p00119

Scholer, M., Fujimoto, M., & Kucharek, H. (1993) Two-dimensional simulations of supercritical quasi-parallel shocks: upstream waves, downstream waves, and shock reformation. J. Geophys. Res. 98, 18971

Sckopke, N., Paschmann, G., Brinca, A.L., Carlson, C. W., & Lühr, H.(1990) Ion thermalization in quasi-perpendicular shocks involving reflected ions. J. Geophys. Res. Volume 95, Issue A5

Siu-Tapia, A., Blanco-Cano, X., Kajdič, P., Aguilar-Rodriguez, E. , Russell, C. T., Jian, L. K., & Luhmann, J. G. (2015), Low-frequency waves within isolated magnetic clouds and complex structures: STEREO observations, J. Geophys. Res. Space Physics,120, 2363-2381, doi:10.1002/2014JA020568

Southwood, D. J., Kivelson, M. G. (1993). Mirror instability. I-Physical mechanism of linear instability. Journal of Geophysical Research 98, 9181.

Sundberg, T., Haynes, C. T., Burgess, D., & Mazelle, C. X. (2016). Ion acceleration at the quasi-parallel bow shock: Decoding the signature of injection. Astrophysical Journal,820, 21

Su, Y., Lu, Q., Gao, X., Huang, C., & Wang, S. (2012a), Ion dynamics at supercritical quasi-parallel shocks: Hybrid simulations, Phys. Plasmas, 19, 092108.

Su, Y., Lu, Q., Huang, C., Wu, M., Gao, X., & Wang, S. (2012b), Particle acceleration and generation of diffuse superthermal ions at a quasi-parallel collisionless shock: Hybrid simulations, J. Geophys. Res., 117, A08107, doi:10.1029/2012JA017736

Trattner, K. J., & Scholer, M. (1991), Diffuse alpha particles upstream of simulated quasi-parallel supercritical collisionless shocks. Geophysical Research Letters, vol. 18, Oct. 1991, p. 1817-1820.

Trattner, K. J., & Scholer, M. (1993) Distributions and thermalization of protons and alpha particles at collisionless quasi-parallel shocks. Annales Geophysicae, Vol. 11, No. 9, p. 774-789

Trattner, K. J. & Scholer, M. (1994) Diffuse minor ions upstream of simulated quasi-parallel shocks. Journal of Geophysical Research, vol. 99, no. A4, p. 6637-6650

Trotta, D. & Burgess, D. (1994) Electron acceleration at quasi-perpendicular shocks in sub and supercritical regimes: 2D and 3D simulations. Monthly Notices of the Royal Astronomical Society, Volume 482, Issue 1, p.1154-1162

Tsubouchi, K., Nagai, T., & Shinohara, I. (2016), Stable ring beam of solar wind He^{2+} in the magnetosheath, J. Geophys. Res.Space Physics,121, 1233-1248, doi:10.1002/2015JA021769

Wilson, L. B. III (2016), Low Frequency Waves at and Upstream of Collisionless Shocks, in Washington DC American Geophysical Union Geophysical Monograph Series, Volume 216, pp.269-291

Winske, D., & Leroy, M. M. (1985), Hybrid simulation techniques applied to the Earth's bow shock, in Computer Simulation of Space Plasmas, edited by H. M. T. Sato, pp. 255-278, Terra Sci., Tokyo, Japan.

Wurz, P. (2005), Solar wind Composition, Proceedings of the 11th European Solar Physics Meeting "The Dynamic Sun: Challenges for Theory and Observations" (ESA SP-600). 11-16 September 2005, Leuven, Belgium. Editors: D. Danesy, S. Poedts, A. De Groof and J. Andries."

Yang, Z. W., Lu, Q. M., Lembège, B., & Wang, S. (2009), Shock front nonstationarity and ion acceleration in supercritical perpendicular shocks, J. Geophys. Res., 114, A03111, doi:10.1029/2008JA013785

Yang, Z. W., Lembège, B., & Lu, Q. M. (2012), Impact of the rippling of a perpendicular shock front on ion dynamics, J. Geophys. Res., 117, A07222, doi:10.1029/2011JA017211

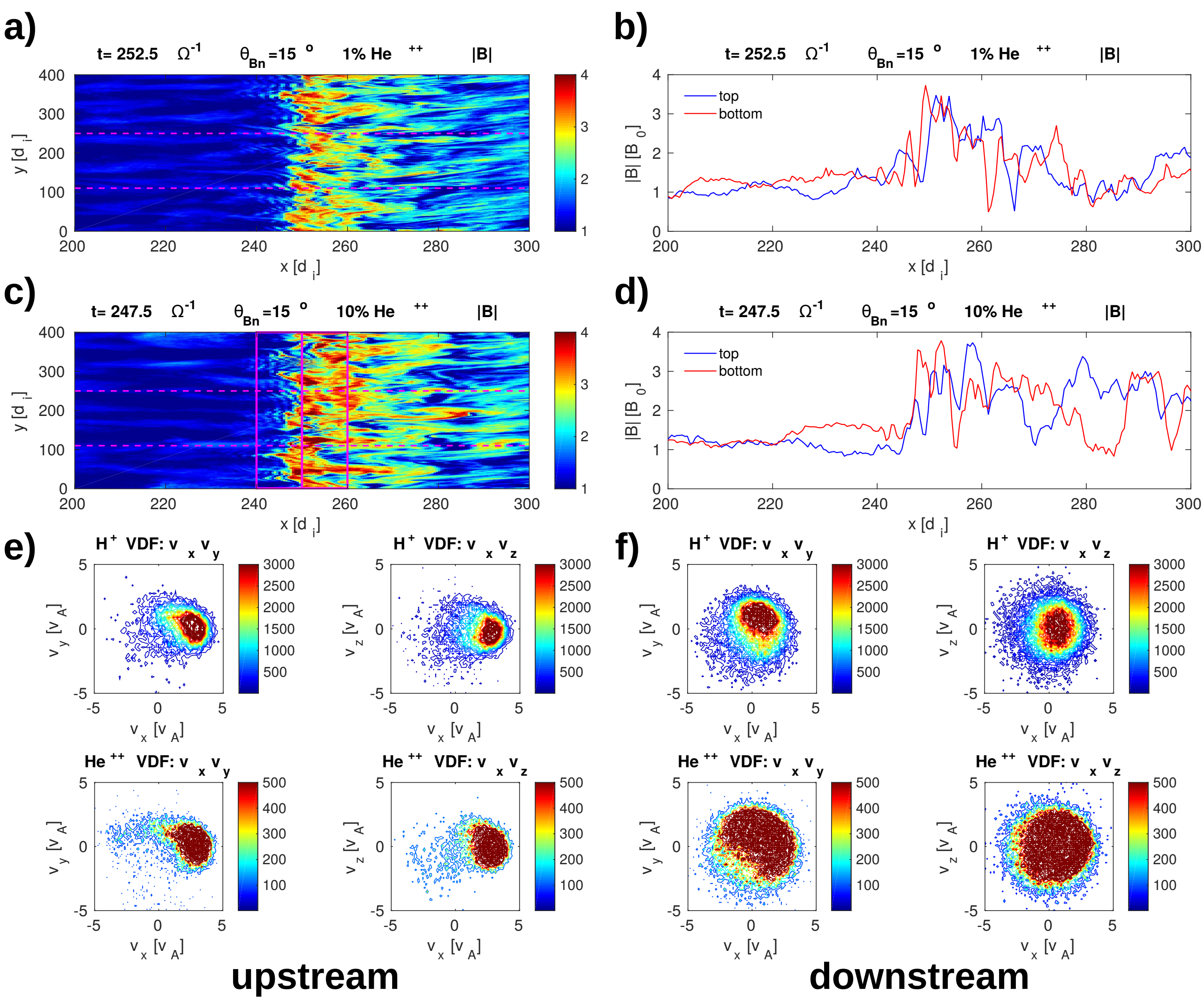

Figure 5. Plots corresponding to the simulation with θ_{Bn}=15° at the time when the shock arrives to x=250 d_i: Contour plot of total magnetic field a) and magnetic field b) along two horizontal cuts at the upper (blue line) and lower (red line) dashed lines in panel a) for the case with 1% of He^{++} particles. Panels c) and d) show the same results for the case with 10% of He^{++} particles. The VDF's for both species for the case with 10% of He^{++} particles contained inside the left (upstream side) magenta box on panel c) are shown in panels e). The same results for the right (downstream side) magenta box on panel c) are shown in panels f). The color bar in VDF's indicates the particle counts.

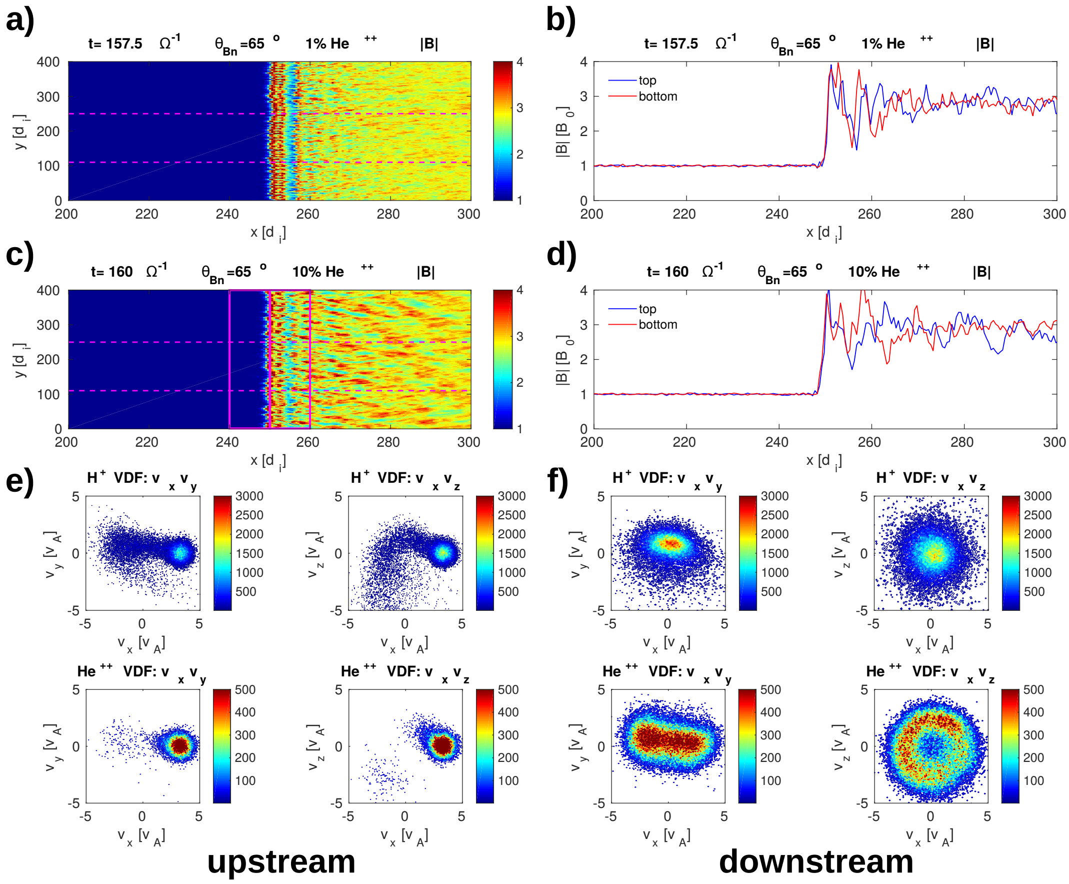

Figure 6. Plots corresponding to the simulation with θ_{Bn}=65° at the time when the shock arrives to x=250 d_i: Contour plot of total magnetic field a) and magnetic field b) along two horizontal cuts at the upper (blue line) and lower (red line) dashed lines in panel a) for the case with 1% of He^{++} particles. Panels c) and d) show the same results for the case with 10% of He^{++} particles. The VDF's for both species for the case with 10% of He^{++} particles contained inside the left (upstream side) magenta box on panel c) are shown in panels e). The same results for the right (downstream side) magenta box on panel c) are shown in panels f). The color bar in VDF's indicates the particle counts.

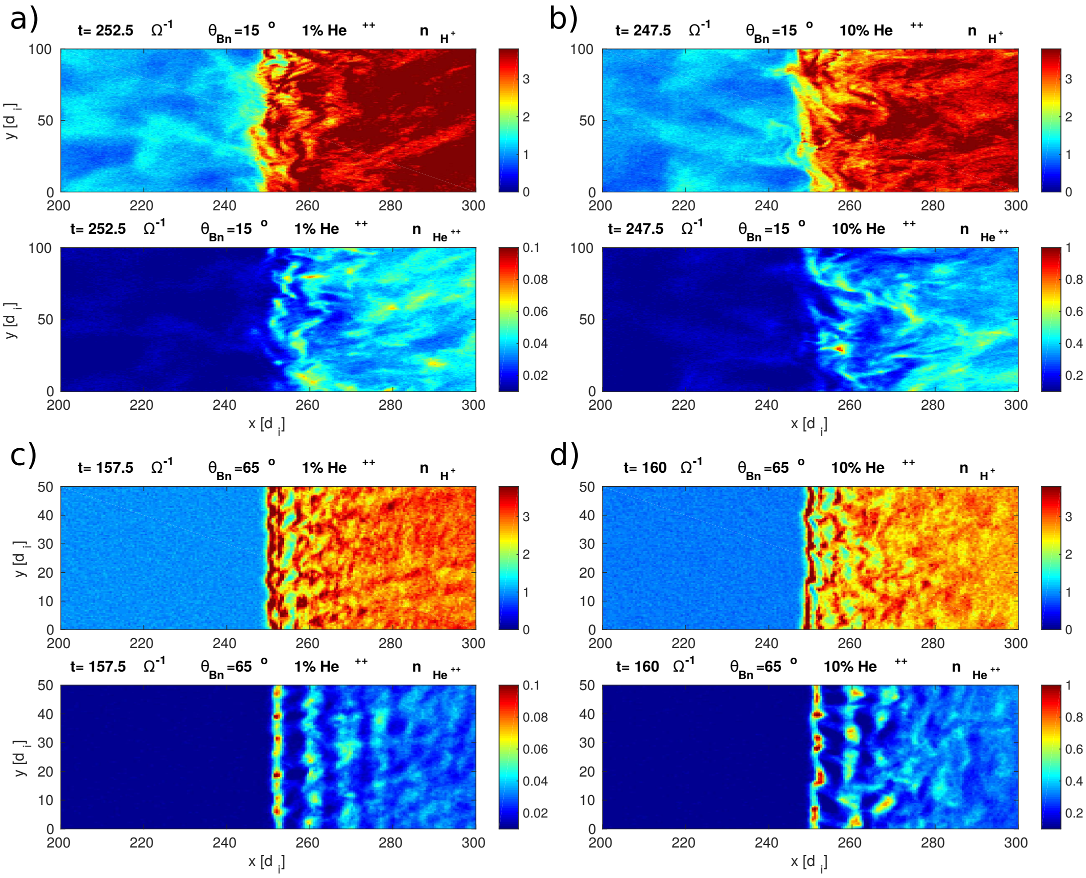

Figure 7. Contour plots of protons and He^{++} densities corresponding to the simulations with $\theta_{Bn} = 15°$ for 1% a) and 10% b) of He^{++} particles and with $\theta_{Bn} = 65°$ for 1% c) and 10% d) of He^{++}. The time of the plots correspond to those magnetic field magnitude plots in Figures 5 and 6.

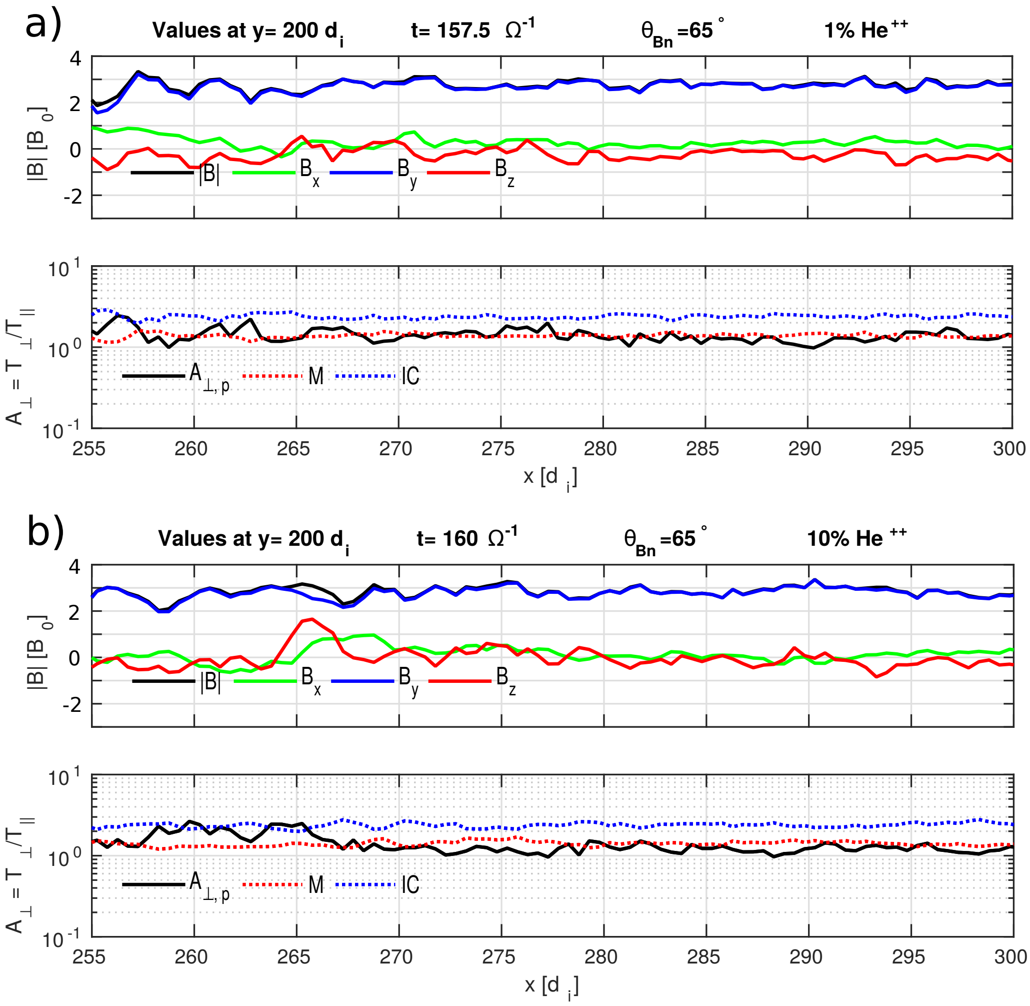

Figure 8. Magnetic field and proton temperature anisotropy ($T_\perp/T_\parallel$) cuts along downstream region at y = 200 d_i corresponding to simulations with θ_{Bn} = 65° for 1% a) and 10% b) of He^{++}. Temperature anisotropy as well as the parameters (M = $1 + 1/\beta_\perp$) in red and (IC = $1 + \beta_\parallel^{0.5}$) in blue are shown in the same panels. The condition for the growing of the mirror instability is fulfilled by the threshold $T_\perp/T_\parallel$ > M, the corresponding condition for ion/cyclotron instability is $T_\perp/T_\parallel$ < IC. The time of the plots correspond to those in Figure 7.